Surface Wave Excitation from Open Microstrip Discontinuities

William P. Harokopus, Jr., *Member, IEEE*, Linda P. B. Katehi, *Senior Member, IEEE*,
Walid Y. Ali-Ahmad, *Student Member, IEEE*, and Gabriel M. Rebeiz, *Member, IEEE*

Abstract —**Radiation properties of open microstrip discontinuities are investigated using a full-wave integral equation technique. The method of moments provides the current distribution over the discontinuity which is used to determine radiation loss. The radiation loss for microstrip bends and stubs is separated into the individual contributions of space and surface wave excitation. Patterns depicting the power propagating in the substrate have been computed and verified experimentally.**

I. Introduction

EXTENSIVE literature has appeared in recent years on the modeling of microstrip discontinuities. At present, models based on static microstrip characteristics (quasi-static models) [1]–[5], dispersion models [6]–[9], and semiempirical results [10] are utilized extensively in commercially available CAD packages. Although adequate at lower frequencies, these models neglect high-frequency electromagnetic interactions and, as a result, may provide inaccurate and even misleading results at submillimeter-wave frequencies. In contrast, full electromagnetic or full-wave techniques [11]–[18] have demonstrated excellent performance in this frequency range owing to the inherent inclusion of these effects. In particular, radiation loss attributed to the excitation of space and surface wave modes has been reported for the open microstrip elements [19], [20] often found in the feeding structures of planar arrays.

In previous work, open microstrip structures were analyzed with the method of moments. Circuit elements were characterized by their network parameters which included total radiation loss. No effort was made to separate this loss into the individual contributions of space and surface waves. Space waves refer to the modes radiated into the semi-infinite region above the dielectric; surface waves are modes bound in the substrate, which forms a grounded dielectric waveguide. In this paper, more specific information about the types and quantity of radiation occurring is presented. These results will provide guidelines for the development of low-loss microstrip elements. For example, it is well known that the shape of discontinuities can be altered to improve circuit performance (e.g. mitered bend, radial stub). However, finding the influence of these and similar modifications on the radiation loss is also important. The technique presented is capable of providing the necessary quantitative results for determining if and why a specific circuit modification decreases radiation loss.

Results will be presented that quantify the radiation occurring from each mechanism and illustrate the directions of propagation of surface wave radiation. These far-field patterns are useful in determining where coupling through surface wave excitation may be strong. In addition, results will be shown demonstrating the strong influence that substrate composition has on radiation properties.

The far-field patterns are obtained in this paper by the complex transformation of the space-domain Green's function to the steepest descent plane, where a saddle point integration is performed. The contribution from the saddle point represents far-field spherical wave power in the half-space above the dielectric. In addition, residues corresponding to the poles captured in the contour deformation represent cylindrical surface waves. Theoretical and experimental results are presented for microstrip stubs and bends that detail the effect of radiation on circuit performance, quantify the types of radiation which are occurring, and show the direction and intensity of surface wave propagation in the substrate.

II. Theory

A. Computation of Current Distribution

A cross section of the microstrip structure is shown in Fig. 1. The conductors are lossless and their thickness is much smaller than a wavelength. The lossless substrate has thickness h. The electric field may be written in terms of the space domain integral equation

$$E(x,y,z)=\iint_{S'}\left[k_i^2\bar{\bar{I}}+\nabla\nabla\right]\cdot\bar{\bar{G}}(x,y,z/x',y',z')\cdot J(s')\,ds',\qquad i=0,1 \quad (1)$$

with k_0 and k_1 being the wavenumbers in free space and the dielectric regions, respectively, and

$$J(s')=J_x(x',y')\hat{x}+J_y(x',y')\hat{y} \quad (2)$$

Manuscript received June 21, 1990; revised February 5, 1991. This work was supported by the National Science Foundation under Contract ECS-8602536.

The authors are with the Electrical Engineering and Computer Science Department, University of Michigan, Ann Arbor, MI 48109.

IEEE Log Number 9144279.

0018-9480/91/0700-1098$01.00 ©1991 IEEE

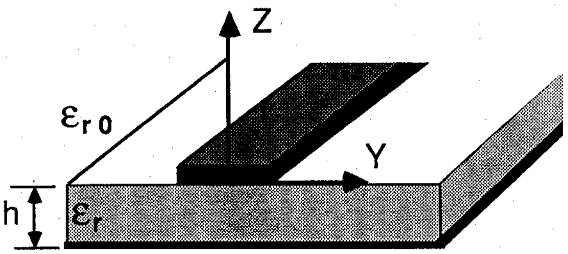

Fig. 1. Open microstrip geometry.

is the current on the conducting strips. The components of the dyadic Green's function

$$\bar{\bar{G}}(x,y,z/x',y',z') = G_{xx}\hat{x}\hat{x} + G_{zx}\hat{z}\hat{x} + G_{yy}\hat{y}\hat{y} + G_{zy}\hat{z}\hat{y} \tag{3}$$

are represented in the form of Sommerfeld integrals [21], and are given to Appendix I.

The microstrip discontinuity is subdivided into rectangles, and the method of moments [22] is applied with rooftop basis functions [23]. These basis functions are consistent with the current boundary conditions, having piecewise-sinusoidal variation in the longitudinal direction and constant variation in the transverse direction.

With the application of Galerkin's method, the integral equation is reduced to a matrix equation

$$[Z][I]=[V]$$

where Z represents the impedance matrix, I is the vector of unknown x and y current amplitudes, and V is the excitation vector which reflects the position of the source. The matrix equation is solved providing the current amplitudes on the discontinuity and the feeding lines. The microstrip structure is excited by infinitesimal gap generators. More details on the excitation and application of the method of moments may be obtained in [18].

B. Far-Field Radiation

The electromagnetic fields generated by the current on the microstrip element may be computed directly from the electric field integral equation after the microstrip current is known. This is done by a numerical integration of (1) after the current summations have been inserted. Performing this integration for the radiated fields at all spatial angles would be extremely time consuming but fortunately is not necessary. To quantify the space and surface wave power losses, it is necessary only to obtain the far-field patterns. These may be obtained by an approximate saddle point integration, which is much less time consuming than a full numerical integration of (1). Of course, to compute the near fields a numerical integration would be required. In this section, the saddle point evaluation for the far fields is presented. As shown in Fig. 2(a), the original path of integration was along the positive real axis. Along this path, a finite number of singularities corresponding to excited surface waves are encountered between the free space (k_0) and the dielectric (k) wavenumbers. To obtain the radiated far fields, the integral is transformed to the steepest descent plane by the complex mapping

$$\lambda = k_0 \sin\alpha. \tag{4}$$

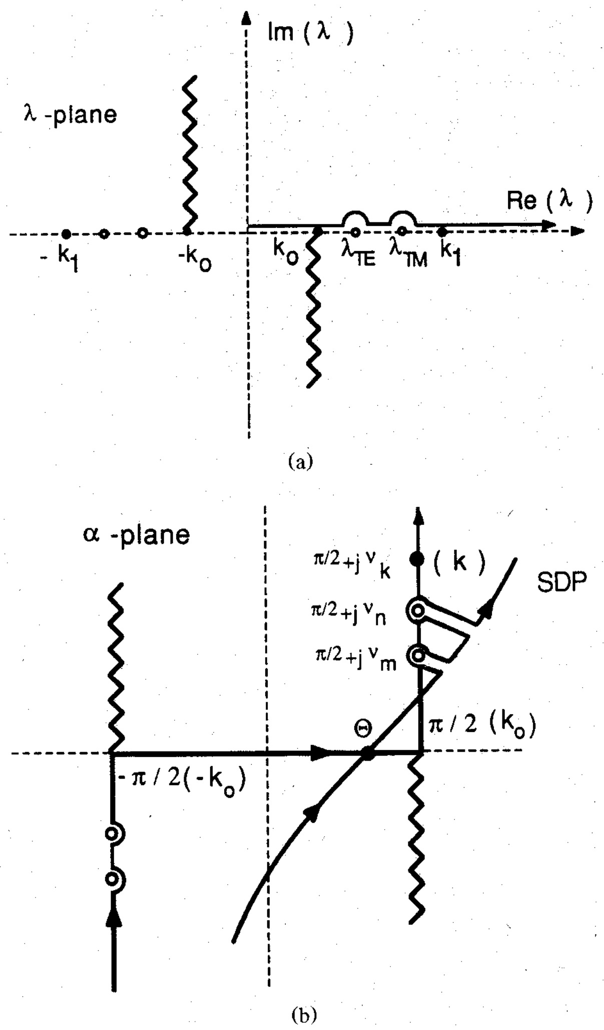

(a)

(b)

Fig. 2. Integration paths: (a) integration along real axis in λ plane; (b) contour of integration in the α plane.

Fig. 2(b) shows the new path of integration in the α plane. The quantities shown in parentheses correspond to the points mapped from the λ plane to the α plane. The poles now lie along the line defined by $\mathrm{Re}(\alpha) = \pi/2$, between the points $\mathrm{Im}(\alpha) = 0$ and $\mathrm{Im}(\alpha) = \nu_k$. The point ν_k is mapped from the point k in the λ plane and has the value

$$\nu_k = \cosh^{-1}(\epsilon_r). \tag{5}$$

Consistent with the far-field approximation, asymptotic approximations are made for the Hankel functions as shown in Appendix II. The contour of integration (Fig. 2(b)) is then deformed into the steepest descent path [24], [26]. A saddle point integration is performed, with the saddle point equal to the spherical observation angle ($\alpha = \theta$). During the contour deformation, a finite number of simple pole singularities are captured as shown. These represent power in the excited surface wave modes and will be discussed in the following section. However, it should be noted that at the cutoff of higher order surface wave modes the pole locations are in close proximity to the saddle point when the observation angle is along the substrate ($\theta = \pi/2$). Consequently, a saddle point analysis in proximity to a simple pole singularity should be performed near cutoff frequencies of higher order modes. As the operating frequency moves away from cutoff, the surface wave pole moves away from the saddle point.

To obtain the fields for a microstrip discontinuity, one returns to the electric field integral equation. In the far field, the electric field can be written in spherical coordinates as

$$E_\theta = k_0^2[\pi_\theta^x + \pi_\theta^y] \tag{6}$$

$$E_\phi = k_0^2[\pi_\phi^x + \pi_\phi^y] \tag{7}$$

with

$$\pi_\theta^x = \int\int_{S'} [G_{xx}\cos(\theta)\cos(\phi) - G_{zx}\sin(\theta)] \cdot J_x(x',y')\,dx'dy'$$

$$\pi_\theta^y = \int\int_{S'} [G_{yy}\cos(\theta)\sin(\phi) - G_{zy}\sin(\theta)] \cdot J_y(x',y')\,dx'dy'$$

$$\pi_\phi^x = \int\int_{S'} [-G_{xx}\sin(\phi)] J_x(x',y')\,dx'dy'$$

$$\pi_\phi^y = \int\int_{S'} [G_{yy}\cos(\phi)] J_y(x',y')\,dx'dy'. \tag{8}$$

Inserting the results of the saddle point analysis (Appendix II) and the values of the microstrip current obtained from the method of moments, the electric field can be written in the form

$$E_\theta = \frac{j\omega\mu_0}{2\pi} k_0^2 \frac{e^{(-jk_0R)}}{k_0R} \cdot \left[\frac{F(\theta)}{f_1(\theta,h)}\cos(\theta) + \frac{jG(\theta)(1-\epsilon_r)}{f_1(\theta,h)f_2(\theta,h)}\sin(\theta)\right] \cdot [A_{rx}(\theta,\phi)\cos(\phi) + A_{ry}(\theta,\phi)\sin(\phi)]$$

$$E_\phi = -\frac{j\omega\mu_0}{2\pi} k_0^2 \frac{e^{(-jk_0R)}}{k_0R}\frac{F(\theta)}{f_1(\theta,h)} \cdot [A_{rx}(\theta,\phi)\sin(\phi) - A_{ry}(\theta,\phi)\cos(\phi)]$$

where the terms $A_{rx}(\theta,\phi)$ and $A_{ry}(\theta,\phi)$ contain the spatial integrations of the basis functions with the Green function's phase terms. These integrations are performed analytically and result in the expressions given below:

$$A_{rx}(\theta,\phi) = 4e^{(jk_0(l/2)\sin(\theta)\sin(\phi))} \cdot \left[\sum_{n=1}^{N+1}\sum_{m=1}^{M+1} I_{nm}^x e^{(jy_mk_0\sin(\theta)\sin(\phi))} e^{(jx_nk_0\sin(\theta)\cos(\phi))}\right] \cdot \frac{\sin\left(k_0\frac{l}{2}\sin(\theta)\sin(\phi)\right)}{k_0\sin(\theta)\sin(\phi)} \cdot \frac{\cos(lk_0\sin(\theta)\cos(\phi)) - \cos(k_sl)}{k_s\sin(k_sl)\left[1-\left(\frac{k_0}{k_s}\right)^2\sin^2(\theta)\cos^2(\phi)\right]} \tag{9}$$

$$A_{ry}(\theta,\phi) = 4e^{(jk_0(l/2)\sin(\theta)\cos(\phi))} \cdot \left[\sum_{n=1}^{N+1}\sum_{m=1}^{M+1} I_{nm}^y e^{(jy_mk_0\sin(\theta)\sin(\phi))} e^{(jx_nk_0\sin(\theta)\cos(\phi))}\right] \cdot \frac{\sin\left(k_0\frac{l}{2}\sin(\theta)\cos(\phi)\right)}{k_0\sin(\theta)\cos(\phi)} \cdot \frac{\cos(lk_0\sin(\theta)\sin(\phi)) - \cos(k_sl)}{k_s\sin(k_sl)\left[1-\left(\frac{k_0}{k_s}\right)^2\sin^2(\theta)\sin^2(\phi)\right]} \tag{10}$$

where the quantities l and k_s represent the subsection length and scaling constant for the basis functions, respectively. More detailed information on the rooftop basis functions is available in [18]. The fields depend on two factors: a substrate contribution, resulting from the Green's function and containing all the information about the substrate; and a shaping contribution, resulting from the spatial dependence of the source and containing all the information about the shape and current distribution over the conducting strips. Consequently, these two factors may be handled independently to reduce loss.

The total far-field space wave power is obtained by integrating the Poynting vector over a hemisphere centered around the discontinuity:

$$P^{sp} = \frac{1}{2}\int_0^{2\pi}\int_0^{\pi/2}\left[\frac{|E_\theta|^2}{\eta_0} + \frac{|E_\phi|^2}{\eta_0}\right] r^2\sin(\theta)\,d\theta\,d\phi. \tag{11}$$

C. Surface Waves

During the contour deformation of the previous section, a finite number of singularities were captured, as shown in Fig. 2. These singularities correspond to excited surface wave modes that fall into two types: transverse electric (TE_z) and transverse magnetic (TM_z) to the dielectric–air interface. The poles are determined by the zeros of two analytic functions present in the denominator of the Green's function given by equations (A12) and (A13).

It is now a simple matter to obtain field patterns in the dielectric ($\theta = \pi/2$) by the application of Cauchy's residue theorem. The total number of poles is determined by the operating frequency and the substrate parameters. The pole locations are given by

$$\alpha_{\mathrm{TM}} = \frac{\pi}{2} + j\nu_n, \qquad n = 1, N_{\mathrm{TM}} \tag{12}$$

$$\alpha_{\mathrm{TE}} = \frac{\pi}{2} + j\nu_m, \qquad m = 1, N_{\mathrm{TE}} \tag{13}$$

where N_{TM} and N_{TE} are the number of excited TM and TE modes, respectively. The far fields are determined by computing the residues of the singularities and are given in Appendix III.

The power in a particular mode is found from the Poynting vector. The surface wave power at the dielectric interface ($Z = 0$) is given by

$$\begin{aligned} P^{\mathrm{TM}}(\phi) = \sum_{n=0}^{N_{\mathrm{TM}}} \frac{k_0^4 \omega \mu_0}{4\pi\rho} & \cdot \frac{\left[\epsilon_r - \cosh^2(\nu_n)\right]\cosh^2(\nu_n)\sinh^2(\nu_n)}{\left|\left[f_2'(\alpha)|_{\pi/2+j\nu_n}\right]\right|^2} \\ & \cdot \sin^2\left[k_0 h\sqrt{\epsilon_r - \cosh^2(\nu_n)}\right] \\ & \cdot \left|\cos(\phi)A_{rx}(\phi) + \sin(\phi)A_{ry}(\phi)\right|^2 \end{aligned} \tag{14}$$

for TM waves and by

$$\begin{aligned} P^{\mathrm{TE}}(\phi) = \sum_{m=0}^{N_{\mathrm{TE}}} \frac{k_0^4 \omega \mu_0}{4\pi\rho} & \frac{\cosh^2(\nu_m)\sinh^2(\nu_m)}{\left|\left[f_1'(\alpha)|_{\pi/2+j\nu_m}\right]\right|^2} \\ & \cdot \sin^2\left[k_0 h\sqrt{\epsilon_r - \cosh^2(\nu_m)}\right] \\ & \cdot \left|\sin(\phi)A_{rx}(\phi) + \cos(\phi)A_{ry}(\phi)\right|^2 \end{aligned} \tag{15}$$

for TE waves. In (14) and (15) the terms $A_{rx}(\phi)$ and $A_{ry}(\phi)$ are given by (9) and (10), with the quantity $k_0 \cosh(\nu_n)$ replacing $k_0 \sin(\theta)$.

The total power in the TM and TE modes may be found by integrating the Poynting vector over a cylindrical surface centered at the discontinuity

$$P^{\mathrm{TM}} = -\int_{-h}^{\infty}\int_0^{2\pi} \frac{E_z \cdot H_\phi^*}{2} \rho \, d\phi \, dz \tag{16}$$

$$P^{\mathrm{TE}} = \int_{-h}^{\infty}\int_0^{2\pi} \frac{E_\phi \cdot H_z^*}{2} \rho \, d\phi \, dz. \tag{17}$$

III. Results

In this section, examples will be presented that quantify the radiation loss for microstrip open-end, radial stub, and bend discontinuities. Additionally, surface wave far-field patterns will be shown for these structures. As mentioned, the surface wave patterns are useful for determining directions of strong coupling between adjacent discontinuities. Space wave far-field patterns have a null along the dielectric substrate, except under rare circumstances (at the cutoff of higher order surface wave modes) which are not applicable to the presented results. Furthermore, surface wave radiation is in the form of cylindrical waves which decay less rapidly with distance than spherical space waves. It is therefore reasonable to conclude that surface waves play a major role in undesirable electromagnetic interference. In addition, the extraction of the exact amount of both types of radiation will help in the design of low-loss elements and extend the use of microstrip circuitry farther into the millimeter-wave region. The first of the following sections will give examples of total surface and space wave losses; the second section includes examples which depict the direction of surface wave propagation.

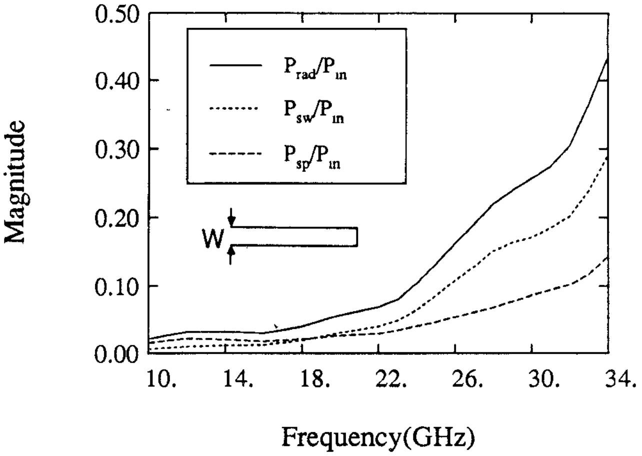

Fig. 3. Radiation loss of open-end stub ($\epsilon_r = 12$, $h = 0.635$ mm, $W = 0.254$ mm).

A. Space and Surface Wave Radiation Losses

1) Stubs: In Fig. 3, the contribution of space and surface waves to total radiation loss is given for an open-ended stub. In the lower frequency range, the space wave contribution is slightly larger. However, the surface wave loss increases sharply with frequency, overtaking the space wave power at 19.5 GHz. Beyond this frequency, the total radiation loss increases sharply owing to a corresponding increase in surface wave loss. The TE_0 mode activates between 35 and 36 GHz, therefore, only one surface wave mode is excited in this example. The total radiation loss approaches half of the input power at 34 GHz, which is a significant amount of loss for an element on a substrate with practical electrical dimensions for (M)MIC applications.

The radial stub is generally utilized for its greater bandwidth. Radiation loss for such a structure is shown in Fig. 4, and exhibits behavior similar to that of the open-ended stub, except that the sharp increase in surface wave and total radiated power is shifted upward. This behavior

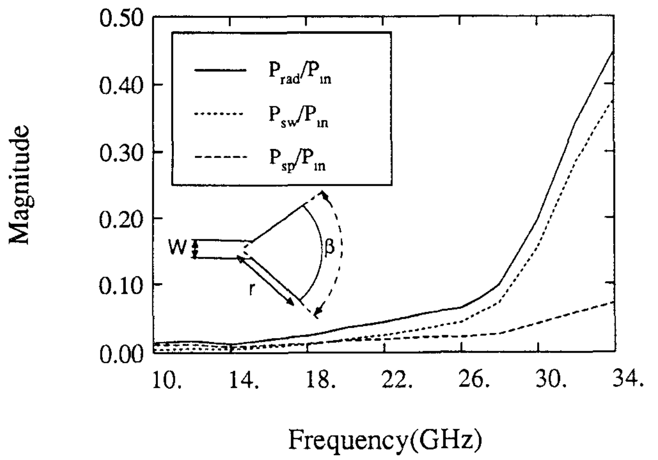

Fig. 4. Radiation loss of radial stub ($\epsilon_r = 12$, $h = 0.635$ mm, $W = 0.254$ mm, $\beta = 90°$, $r = 0.889$ mm).

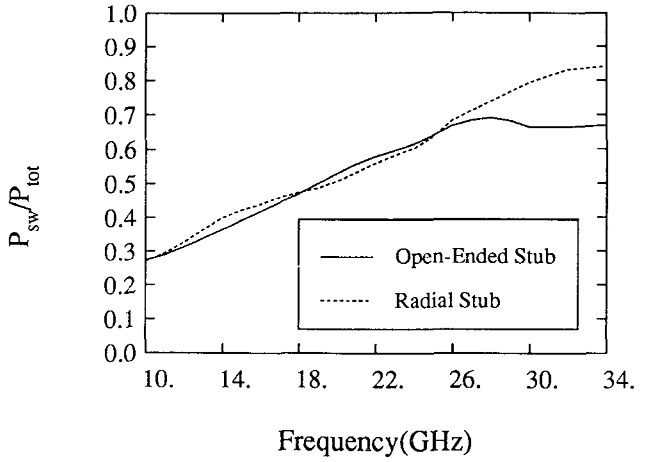

Fig. 5. Percentage of surface wave loss ($P_{tot} = P_{sw} + P_{sp}$) from open-ended and radial stubs ($\epsilon_r = 12$, $h = 0.635$ mm, $W = 0.254$ mm).

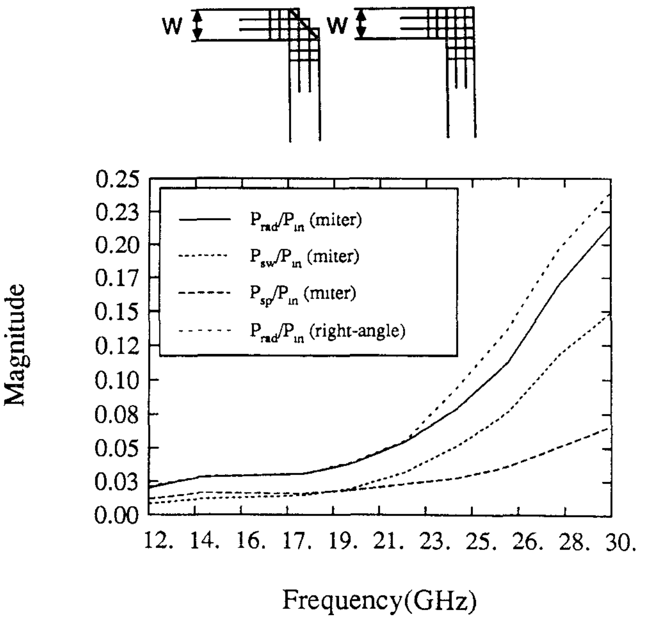

Fig. 6. Radiation loss of mitered bend ($\epsilon_r = 12$, $h = 0.635$ mm, $W = 0.381$ mm).

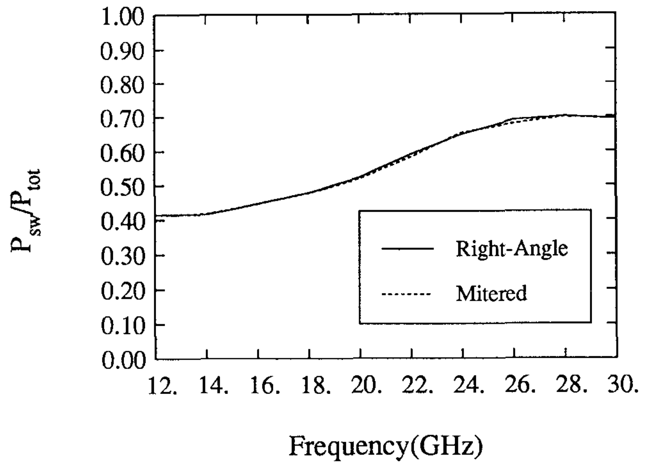

Fig. 7. Percentage of surface wave loss ($P_{tot} = P_{sw} + P_{sp}$) from mitered and right-angle bends ($\epsilon_r = 12$, $h = 0.635$ mm, $W = 0.381$ mm).

results in less radiation loss in the 20–30 GHz range of operation. In both of the above examples, the radiation loss will continue to increase until the first higher order mode is excited, and then it will oscillate as reported in [25]. Although the shape of the metallization has a strong influence on the total loss, it does not appear to have a greater influence on either of the two types of lower frequencies, as shown in Fig. 5. However, above 30 GHz the radial stub radiates a higher percentage of power into the excited surface wave mode.

2) Mitered Bend: Chamfering of microstrip bends is a common practice for the reduction of input VSWR. The example shown in Fig. 6 clearly illustrates that mitering can result in lower radiation loss as well. The losses between the mitred and right-angle bend are effectively equal until 20 GHz ($h = 0.127\lambda_g$). Beyond this frequency, the right-angle bend clearly radiates more power. Fig. 6 also shows that, once again, the radiation is dominated by surface waves at high frequencies. However, the mitering produces a reduction in both space and surface wave power as illustrated in Fig. 7, where both the mitered and unmitered cases exhibit identical percentages of surface wave loss. Mitering effectively increases the useful range of operation of the bend element by decreasing the radiation loss. A similar discontinuity printed on a substrate of lower permittivity would exhibit lower, but still significant, surface wave losses.

B. Surface Wave Patterns

The preceding analysis was utilized to obtain patterns in the substrate for the TM_0 surface wave mode. As previously mentioned, this mode is excited at any operating frequency. Accordingly, it is important to know its direction and the amount of power propagating. Theoretical and experimental patterns were obtained at 10 GHz for microstrip stub and bend discontinuities printed on a 96 mil (2.44 mm) Duroid ($\epsilon_r = 2.3$) substrate. The Duroid

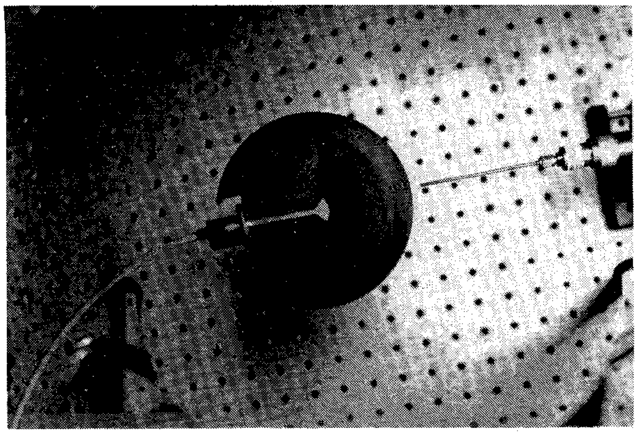

Fig. 8. Microstrip radial stub printed on Duroid substrate ($\epsilon_r = 2.3$, $h = 2.44$ mm, $W = 2.54$ mm).

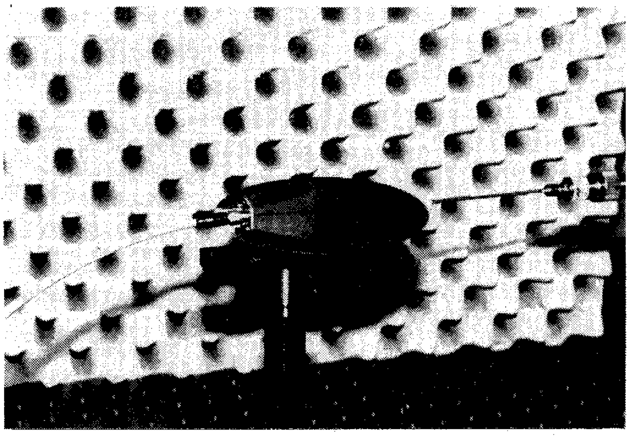

Fig. 9. Experimental setup for surface wave pattern measurements ($\epsilon_r = 2.3$, $h = 2.44$ mm, $W = 2.54$ mm).

substrates were machined into 5-in.-diameter circular sections, shown in Fig. 8, with the substrate edges gradually tapered to minimize the reflection of the surface wave at the edge of the substrate. The microstrip element, in this case a radial stub, was etched from the copper metallization on the top face of the substrate. The experimental setup is shown in Fig. 9. The substrates were elevated onto a rotating pedestal and surrounded by absorber to minimize multiple reflections. Each element was fed at the edge of the substrate with a 10 GHz signal and a resonant dipole was positioned near the edge to measure the pattern. The distance from the launcher to the discontinuity is 50 mm. The pedestal was then rotated to alter the observation angle (ϕ). Absorber was placed over the microstrip launcher to minimize extraneous radiation. A similar technique was employed to measure surface wave fields of coplanar waveguide discontinuities in [28].

1) Open-Ended and Radial Stub: The experimental results for a 100 Ω ($W = 2.54$ mm) open-ended line were compared with the theoretical results derived by the previously presented method. Fig 10 shows that the theoretical results agree well with the experimental results. The open-ended line radiates power in the TM_0 surface wave along the longitudinal axis of the line. The experimental and theoretical results include the effect of finite feed line length, as demonstrated by the side lobes in the pattern.

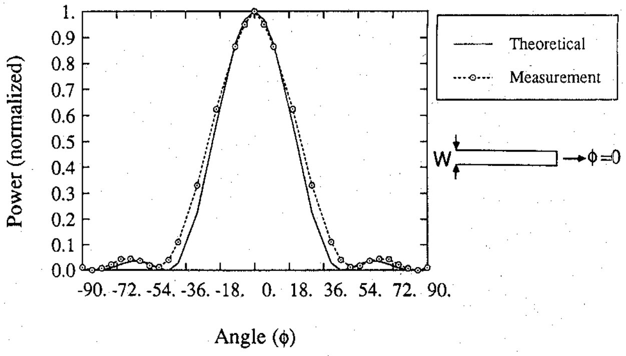

Fig. 10. Surface wave pattern of open-ended line ($\epsilon_r = 2.3$, $h = 2.44$ mm, $W = 2.54$ mm).

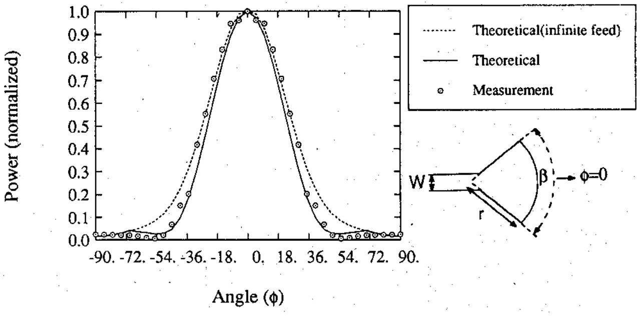

Fig. 11. Surface wave pattern of radial stub ($\epsilon_r = 2.3$, $h = 2.44$ mm, $W = 2.54$ mm, $r = 10.16$ mm, $\beta = 90°$).

The TM_0 surface wave pattern of the previously shown radial stub was also measured. The 10.16 mm radial portion swept out an angle of 90° and was fed by a 100 Ω microstrip line. As mentioned, radial stubs are useful as broader band elements in (M)MIC design. Fig. 11 shows the excellent agreement between theoretical and experimental results. The results are very similar to those obtained for the open-ended line, with the surface wave power excited along the longitudinal axis. However, despite having a larger aperture, the radial stub has a wider beam width than the open-ended line. This occurs because a quadratic phase is present along the aperture, which also results in the filling of the nulls shown by both the theory and experiment.

The theoretical pattern of a radial stub which is fed by a semi-infinite length of feed line is also shown. As can be seen, the side lobes are no longer present and the beam width was widened.

2) Bend Discontinuity: A two-port right-angle bend discontinuity, shown in Fig. 12, was fabricated and measured. Experimentally, port 2 was left open ended at 50 mm ($\simeq 2\lambda_0$) from the bend discontinuity. The theoretical model assumed a semi-infinite feed line (shown as direction $\phi = 0$ in picture), and assumed that the second port was left open ended but extended far from the discontinuity. This extension maintains the standing wave ratio on

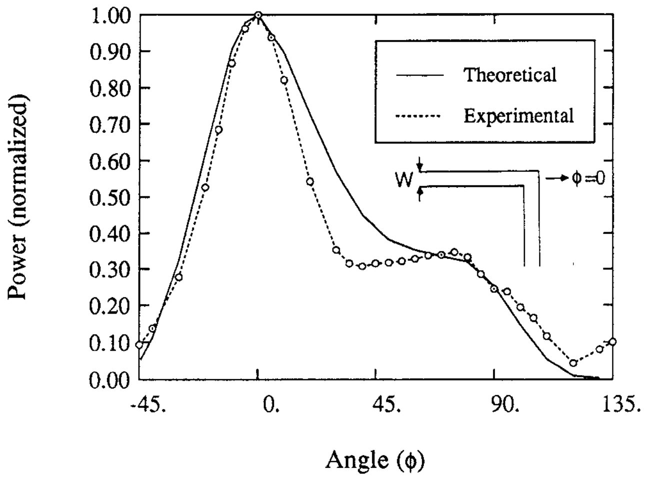

Fig. 12. Surface wave pattern of right-angle bend ($\epsilon_r = 2.3$, $h = 2.44$ mm, $W = 2.54$ mm).

the line but removes the radiation from the open, thereby isolating the radiation pattern of the bend. As shown in Fig. 12, the agreement between theory and experiment is good. The experimental results show the combined effects of finite feed line length and the radiation from the open end. This results in the discrepancy between the theory and experiment around 45°. Since the experiment was designed to measure the bend pattern, the open-end discontinuity was positioned at the edge of the substrate in the experimental model to minimize its effects, and could not be accurately incorporated into the theoretical computation. The side lobe present at about 90° in both the theoretical and experimental results comes from the power reflected at the open end which returns to the bend and radiates there. This lobe would be smaller if the second port were matched.

IV. CONCLUSION

Formulas have been presented to characterize power loss from open microstrip discontinuities. The technique utilizes microstrip current distributions obtained with the method of moments. The formulas allow the separation of total loss into the individual contributions of space wave and surface wave radiation and indicate the direction in which surface wave power is propagating within the substrate. Results presented show that, on high-density substrates, high-frequency radiation loss is dominated by the TM_0 surface wave. This mode is excited in the direction of the longitudinal axis of the stub and bend discontinuities shown, and may have a narrow beam width. A novel experimental approach was used to verify these surface wave patterns.

A specific example of a mitered bend was shown to radiate less power than its right-angle counterpart. Such a minor topology change had a significant influence on total radiated power, without having a more significant impact on either of the two types. This is reflected in an equal percentage reduction in both space and surface wave radiation. It is known, from published work on microstrip antennas, that the substrate structure plays an important role in surface wave radiation. Therefore, an element showing improves loss performance on a single layer, such as the mitered bend, will show further improvement when printed on a multiple-layer substrate designed to have lower substrate losses.

APPENDIX I

The components of the space domain Green's function are given by

$$G_{xx} = G_{yy} = -\frac{j\omega\mu_0}{2\pi k_0^2}$$

$$\cdot \int_0^\infty J_0(\lambda\rho)\frac{\sinh(uh)}{f_1(\lambda,h)}e^{-u_0 z}\lambda\, d\lambda \qquad (Z>0)$$

$$G_{zx} = \cot(\phi)G_{zy}$$

$$= -\frac{j\omega\mu_0}{2\pi k_0^2}(1-\epsilon_r)\cos\phi\int_0^\infty J_1(\lambda\rho)e^{-u_0 z}$$

$$\cdot \frac{\sinh(uh)\cosh(uh)}{f_1(\lambda,h)f_2(\lambda,h)}\lambda^2 d\lambda \qquad (Z>0)$$

$$G_{xx} = G_{yy}$$

$$= -\frac{j\omega\mu_0}{2\pi k^2}\int_0^\infty J_0(\lambda\rho)\frac{\sinh u(z+h)}{f_1(\lambda,h)}\lambda\, d\lambda \qquad (Z<0)$$

$$G_{zx} = \cot(\phi)G_{zy}$$

$$= -\frac{j\omega\mu_0}{2\pi k^2}(1-\epsilon_r)\cos\phi\int_0^\infty J_1(\lambda\rho)$$

$$\cdot \frac{\sinh(uh)\cosh u(z+h)}{f_1(\lambda,h)f_2(\lambda,h)}\lambda^2 d\lambda \qquad (Z<0) \quad \text{(A1)}$$

with $\rho = \sqrt{(x-x')^2+(y-y')^2}$, $u_0 = \sqrt{\lambda^2 - k_0^2}$, and $u_1 = \sqrt{\lambda^2 - k_1^2}$. The equations $f_1(\lambda,h)$ and $f_2(\lambda,h)$ represent characteristic equations for surface wave modes given by

$$f_1(\lambda,h) = u_0\sinh(uh) + u\cosh(uh) \qquad \text{(A2)}$$

$$f_2(\lambda,h) = \epsilon_r u_0\cosh(uh) + u\sinh(uh) \qquad \text{(A3)}$$

where ϵ_r is the relative dielectric constant and h is the thickness of the substrate.

These components of the Green's function may also be represented as infinite integrations through the relationships

$$J_0(\lambda\rho) = \frac{1}{2}\left[H_0^{(1)}(\lambda\rho) + H_0^{(2)}(\lambda\rho)\right] \qquad \text{(A4)}$$

$$J_1(\lambda\rho) = \frac{1}{2}\left[H_1^{(1)}(\lambda\rho) + H_1^{(2)}(\lambda\rho)\right] \qquad \text{(A5)}$$

$$H_0^{(2)}(\lambda\rho) = -H_0^{(1)}(-\lambda\rho) \qquad \text{(A6)}$$

$$H_1^{(2)}(\lambda\rho) = H_1^{(1)}(-\lambda\rho) \qquad \text{(A7)}$$

which result in the expressions in the free-space region

$(z > 0)$:

$$G_{xx} = G_{yy} = -\frac{j\omega\mu_0}{4\pi k_0^2}\int_{-\infty}^{\infty} H_0^{(1)}(\lambda\rho)e^{-u_0 z}\frac{\sinh(uh)}{f_1(\lambda,h)}\lambda\, d\lambda$$

$$G_{zx} = \cot\phi G_{zy}$$

$$= -\frac{j\omega\mu_0}{4\pi k_0^2}(1-\epsilon_r)\cos\phi\int_{-\infty}^{\infty} H_1^{(1)}(\lambda\rho)e^{-u_0 z}$$

$$\cdot\frac{\sinh(uh)\cosh(uh)}{f_1(\lambda,h)f_2(\lambda,h)}\lambda^2\, d\lambda. \qquad \text{(A8)}$$

APPENDIX II

To find the far-field patterns above the dielectric, the components of the Green's function are more appropriately given in spherical coordinates according to

$$\rho = r\sin\theta \qquad \text{(A9)}$$

$$z = r\cos\theta. \qquad \text{(A10)}$$

After substitution of (A9) and (A10) into (A8), the form of the Green's function becomes

$$G_{xx} = G_{yy} = -\frac{j\omega\mu_0}{4\pi k_0^2}\int_{-\infty}^{\infty} H_0^{(1)}(rk_0\sin(\theta)\sin(\alpha))$$

$$\cdot e^{-jk_0 r\cos(\theta)\cos(\alpha)}$$

$$\cdot\frac{j\sin\left(k_0 h\sqrt{\epsilon_r-\sin^2(\alpha)}\right)}{f_1(\alpha)}$$

$$\cdot k_0^2\cos(\alpha)\sin(\alpha)\, d\alpha$$

$$G_{zx} = \cot\phi G_{zy} = -\frac{j\omega\mu_0}{4\pi k_0^2}(1-\epsilon_r)\cos(\phi)$$

$$\cdot\int_{-\infty}^{\infty} H_1^{(1)}(rk_0\sin(\theta)\sin(\alpha))e^{-jk_0 r\cos(\theta)\cos(\alpha)}$$

$$\cdot\frac{j\sin\left(k_0 h\sqrt{\epsilon_r-\sin^2(\alpha)}\right)\cos\left(k_0 h\sqrt{\epsilon_r-\sin^2(\alpha)}\right)}{f_1(\alpha)f_2(\alpha)}$$

$$\cdot k_0^3\cos(\alpha)\sin^2(\alpha)\, d\alpha \qquad \text{(A11)}$$

where the surface wave characteristic equations become

$$f_1(\alpha) = -k_0\cos(\alpha)\sin\left(k_0 h\sqrt{\epsilon_r-\sin^2(\alpha)}\right)$$

$$+ jk_0\sqrt{\epsilon_r-\sin^2(\alpha)}\cos\left(k_0 h\sqrt{\epsilon_r-\sin^2(\alpha)}\right) \qquad \text{(A12)}$$

for TE surface waves and

$$f_2(\alpha) = -k_0\sqrt{\epsilon_r-\sin^2(\alpha)}\sin\left(k_0 h\sqrt{\epsilon_r-\sin^2(\alpha)}\right)$$

$$+ jk_0\epsilon_r\cos(\alpha)\cos\left(k_0 h\sqrt{\epsilon_r-\sin^2(\alpha)}\right) \qquad \text{(A13)}$$

for TM surface waves. Far-field patterns ($rk_0 \gg 1$) are desired. Under this condition, the Hankel functions may be replaced by their respective large argument approximations,

$$H_0^{(1)}(rk_0\sin(\theta)\sin(\alpha)) \simeq \sqrt{\frac{2j}{\pi rk_0}}\frac{e^{-jrk_0\sin(\theta)\sin(\alpha)}}{\sqrt{\sin(\alpha)\sin(\theta)}} \qquad \text{(A14)}$$

$$H_1^{(1)}(rk_0\sin(\theta)\sin(\alpha)) \simeq \sqrt{\frac{2j}{\pi rk_0}}\frac{je^{-jrk_0\sin(\theta)\sin(\alpha)}}{\sqrt{\sin(\alpha)\sin(\theta)}} \qquad \text{(A15)}$$

resulting in the final expressions

$$G_{xx} = G_{yy} = -\frac{j\omega\mu_0}{4\pi}\sqrt{\frac{2j}{\pi rk_0}}\int_{-\infty}^{\infty}\frac{jF(\alpha)}{f_1(\alpha)}e^{-jk_0 r\cos(\theta-\alpha)}\, d\alpha \qquad \text{(A16)}$$

$$G_{zx} = \cot\phi G_{zy} = -\frac{j\omega\mu_0}{4\pi}\sqrt{\frac{2j}{\pi rk_0}}(1-\epsilon_r)\cos(\phi)$$

$$\cdot\int_{-\infty}^{\infty}\frac{G(\alpha)e^{-jk_0 r\cos(\theta-\alpha)}}{f_1(\alpha)f_2(\alpha)}\, d\alpha \qquad \text{(A17)}$$

with

$$F(\alpha) = \frac{\sin(\alpha)\cos(\alpha)}{\sqrt{\sin(\theta)\sin(\alpha)}}\sin\left(k_0 h\sqrt{\epsilon_r-\sin^2(\alpha)}\right) \qquad \text{(A18)}$$

$$G(\alpha) = -\frac{k_0\sin(\alpha)^2\cos(\alpha)}{\sqrt{\sin(\theta)\sin(\alpha)}}\sin\left(k_0 h\sqrt{\epsilon_r-\sin^2(\alpha)}\right)$$

$$\cdot\cos\left(k_0 h\sqrt{\epsilon_r-\sin^2(\alpha)}\right). \qquad \text{(A19)}$$

The contour is deformed into the steepest descent path as described in the main text with the saddle point being the observation angle ($\alpha = \theta$). The contribution from the saddle point is of the form

$$G_{xx} = \frac{j\omega\mu_0}{2\pi}\frac{e^{(-jk_0 R)}}{k_0 R}\frac{F(\theta)}{f_1(\theta,h)}$$

$$\cdot e^{(jk_0[x'\sin(\theta)\cos(\phi)+y'\sin(\theta)\sin(\phi)])} \qquad \text{(A20)}$$

$$G_{zx} = -\frac{j\omega\mu_0}{2\pi}(1-\epsilon_r)\cos(\phi)\frac{e^{(-jk_0 R)}}{k_0 R}\frac{jG(\theta)}{f_1(\theta,h)f_2(\theta,h)}$$

$$\cdot e^{(jk_0[x'\sin(\theta)\cos(\phi)+y'\sin(\theta)\sin(\phi)])}. \qquad \text{(A21)}$$

These expressions give the far-field patterns above the substrate (space wave patterns). They are spherical waves as seen by their spatial dependence $e^{(-jk_0 R)}/k_0 R$. In the phase terms of the above expressions

$$R = r + (x'\sin(\theta)\cos(\phi) + y'\sin(\theta)\sin(\phi)),$$

and the amplitude terms $1/r$ have been replaced by $1/R$.

APPENDIX III

This appendix deals with surface wave fields resulting from application of Cauchy's theorem. For the TM case,

$$E_z = \frac{k_0^2 \omega \mu_0}{2} \sqrt{\frac{2j}{\pi \rho k_0}} \cos(\phi) \cdot \sum_{n=0}^{N_{\mathrm{TM}}} \frac{\sqrt{\epsilon_r - \cosh^2(\nu_n)}}{\sqrt{\cosh \nu_n}} \frac{\cosh^2(\nu_n) \sinh(\nu_n)}{[f_1'(\alpha, h)]|_{\pi/2 + j\nu_n}} \cdot \sin\left[k_0 \sqrt{\epsilon_r - \cosh^2(\nu_n)}\, h\right] e^{-jk_0 \rho \cosh(\nu_n)} e^{-k_0 z \sinh(\nu_n)} \quad (Z > 0) \quad \text{(A22)}$$

$$H_\phi = -\frac{k_0^3}{2} \sqrt{\frac{2j}{\pi \rho k_0}} \cos(\phi) \cdot \sum_{n=0}^{N_{\mathrm{TM}}} \frac{\sqrt{\epsilon_r - \cosh^2(\nu_n)}}{\sqrt{\cosh \nu_n}} \frac{\cosh(\nu_n) \sinh(\nu_n)}{[f_2'(\alpha, h)]|_{\pi/2 + j\nu_n}} \cdot \sin\left[k_0 \sqrt{\epsilon_r - \cosh^2(\nu_n)}\, h\right] e^{-jk_0 \rho \cosh(\nu_n)} e^{-k_0 z \sinh(\nu_n)} \quad (Z > 0) \quad \text{(A23)}$$

$$E_z = \frac{k_0^2 \omega \mu_0}{2} \sqrt{\frac{2j}{\pi \rho k_0}} \cos(\phi) \cdot \sum_{n=0}^{N_{\mathrm{TM}}} \frac{\cosh^2(\nu_n) \sinh^2(\nu_n)}{\sqrt{\cosh \nu_n}} e^{-jk_0 \rho \cosh(\nu_n)} \cdot \frac{\cos\left[k_0 \sqrt{\epsilon_r - \cosh^2(\nu_n)}\, (z + h)\right]}{[f_2'(\alpha, h)]|_{\pi/2 + j\nu_n}} \quad (Z < 0) \quad \text{(A24)}$$

$$H_\phi = -\frac{j\epsilon_r k_0^3}{2} \sqrt{\frac{2j}{\pi \rho k_0}} \cos(\phi) \cdot \sum_{n=0}^{N_{\mathrm{TM}}} \frac{\cosh(\nu_n) \sinh^2(\nu_n)}{\sqrt{\cosh \nu_n}} e^{-jk_0 \rho \cosh(\nu_n)} \cdot \frac{\cos\left[k_0 \sqrt{\epsilon_r - \cosh^2(\nu_n)}\, (z + h)\right]}{[f_2'(\alpha, h)]|_{\pi/2 + j\nu_n}} \quad (Z < 0). \quad \text{(A25)}$$

And for the TE case,

$$H_z = \frac{k_0^3}{2} \sqrt{\frac{2j}{\pi \rho k_0}} \sin(\phi) \cdot \sum_{m=0}^{N_{\mathrm{TE}}} \frac{\cosh^2(\nu_m) \sinh(\nu_m)}{\sqrt{\cosh \nu_m}\, [f_1'(\alpha, h)]|_{\pi/2 + j\nu_m}} \cdot \sin\left[k_0 \sqrt{\epsilon_r - \cosh^2(\nu_m)}\, h\right] e^{-jk_0 \rho \cosh(\nu_m)} \cdot e^{-k_0 z \sinh(\nu_m)} \quad (Z > 0) \quad \text{(A26)}$$

$$E_\phi = \frac{k_0^2 \omega \mu_0}{2} \sqrt{\frac{2j}{\pi \rho k_0}} \sin(\phi) \cdot \sum_{m=0}^{N_{\mathrm{TE}}} \frac{\cosh(\nu_m) \sinh(\nu_m)}{\sqrt{\cosh \nu_m}\, [f_1'(\alpha, h)]|_{\pi/2 + j\nu_m}} \cdot \sin\left[k_0 \sqrt{\epsilon_r - \cosh^2(\nu_m)}\, h\right] e^{-jk_0 \rho \cosh(\nu_m)} \cdot e^{-k_0 z \sinh(\nu_m)} \quad (Z > 0) \quad \text{(A27)}$$

$$H_z = \frac{k_0^3}{2} \sqrt{\frac{2j}{\pi \rho k_0}} \sin(\phi) \cdot \sum_{m=0}^{N_{\mathrm{TE}}} \frac{\cosh^2(\nu_m) \sinh(\nu_m)}{\sqrt{\cosh \nu_m}\, [f_1'(\alpha, h)]|_{\pi/2 + j\nu_m}} e^{-jk_0 \rho \cosh(\nu_m)} \cdot \sin\left[k_0 \sqrt{\epsilon_r - \cosh^2(\nu_m)}\, (z + h)\right] \quad (Z < 0) \quad \text{(A28)}$$

$$E_\phi = \frac{k_0^2 \omega \mu_0}{2} \sqrt{\frac{2j}{\pi \rho k_0}} \sin(\phi) \cdot \sum_{m=0}^{N_{\mathrm{TE}}} \frac{\cosh(\nu_m) \sinh(\nu_m)}{\sqrt{\cosh \nu_m}\, [f_1'(\alpha, h)]|_{\pi/2 + j\nu_m}} e^{-jk_0 \rho \cosh(\nu_m)} \cdot \sin\left[k_0 \sqrt{\epsilon_r - \cosh^2(\nu_m)}\, (z + h)\right] \quad (Z < 0). \quad \text{(A29)}$$

REFERENCES

[1] M. Maeda, "Analysis of gap in microstrip transmission lines," *IEEE Trans. Microwave Theory Tech.*, vol. MTT-20, pp. 390–396, Jun. 1972.

[2] P. Benedek and P. Silvester, "Equivalent capacitance of microstrip gaps and steps," *IEEE Trans. Microwave Theory Tech.*, vol. MTT-20, pp. 729–733, Nov. 1972.

[3] P. Silvester and P. Benedek, "Equivalent capacitance of microstrip open circuits," *IEEE Trans. Microwave Theory Tech.*, vol. MTT-20, pp. 511–516, Aug. 1972.

[4] P. Silvester and P. Benedek, "Equivalent discontinuities capacitances for right-angle bends, T-junctions, and crossings," *IEEE Trans. Microwave Theory Tech.*, vol. MTT-21, pp. 341–346, May 1973.

[5] R. Horton, "The electrical characterization of a right-angle bend in microstrip line," *IEEE Trans. Microwave Theory Tech.*, Vol. MTT-21, pp. 427–429, Jun. 1973.

[6] T. Itoh, "Analysis of microstrip resonators," *IEEE Trans. Microwave Theory Tech.*, vol. MTT-22, pp. 946–952, Nov. 1974.

[7] I. Wolff, G. Kompa, and R. Mehran, "Calculation method for microstrip discontinuities and T-junctions," *Electron. Lett.*, vol. 8, 1972.

[8] G. Kompa and R. Mehran, "Planar waveguide model for calculating microstrip components," *Electron. Lett.*, vol. 11, 1975.

[9] W. Menzel and I. Wolff, "A method for calculating the frequency dependent properties of microstrip discontinuities," *IEEE Trans. Microwave Theory Tech.*, vol. MTT-25, pp. 107–112, Feb. 1977.

[10] M. Kirschning, R. H. Jansen, and H. L. Koster, "Measurement and computer-aided modeling of microstrip discontinuities by an improved resonator method," in *1983 IEEE MTT-S Int. Microwave Symp. Dig.*, May, 1983.

[11] P. B. Katehi and N. G. Alexopoulos, "On the effect of substrate thickness and permittivity on printed circuit dipole performance," *IEEE Trans. Antennas Propagat.*, vol. AP-31, pp. 34–38, Jan. 1983.

[12] V. G. Alexopoulos, P. B. Katehi, and D. Rutledge, "Substrate optimization of integrated circuit applications," *IEEE Trans. Microwave Theory Tech.*, vol. MTT-31, pp. 550–557, July 1983.

[13] P. B. Katehi and N. G. Alexopoulos, "Frequency-dependent characteristics of microstrip discontinuities in millimeter-wave integrated circuits," *IEEE Trans. Microwave Theory Tech.*, vol. MTT-33, pp. 1029–1035, Oct. 1985.

[14] J. R. Mosig, "Arbitrarily shaped microstrip structures and their analysis with a mixed potential integral equation," *IEEE Trans. Microwave Theory Tech.*, vol. 36, pp. 314–323, Feb. 1988.

[15] R. W. Jackson and D. M. Pozar, "Full-wave analysis of microstrip open-end and gap discontinuities," *IEEE Trans. Microwave Theory Tech.*, vol. MTT-33, pp. 1036–1042, Oct. 1985.

[16] R. H. Jansen, "The spectral domain approach for microwave integrated circuits," *IEEE Trans. Microwave Theory Tech.*, vol. MTT-33, pp. 1043–1056, Oct. 1985.

[17] R. Jackson, "Full-wave finite element analysis of irregular microstrip discontinuities," *IEEE Trans. Microwave Theory Tech.*, vol. 37, pp. 81–89, Jan. 1989.

[18] W. P. Harokopus, Jr. and P. B. Katehi, "Characterization of open microstrip discontinuities on multilayer substrates including radiation losses," *IEEE Trans. Microwave Theory Tech.*, vol. 37, pp. 1964–1972, Dec. 1989.

[19] W. P. Harokopus, Jr. and P. B. Katehi, "Radiation properties of microstrip discontinuities," in *IEEE AP Dig.*, June 1989.

[20] T. S. Horng, S. C. Wu, H. Y. Yang and N. G. Alexopoulos, "A generalized method for the distinction of radiation and surface wave losses in microstrip discontinuities," in *IEEE MTT-S Int. Microwave Symp. Dig.*, May 1990, pp. 1055–1058.

[21] A. Sommerfeld, *Partial Differential Equations in Physics.* New York: Academic Press, 1949.

[22] R. F. Harrington, *Field Computation By Moment Methods.* New York: Macmillan, 1968.

[23] J. C. Rautio and R. F. Harrington, "An electromagnetic timeharmonic analysis of shielded microstrip circuits," *IEEE Trans. Microwave Theory Tech.*, vol. MTT-35, pp. 726–730, Aug. 1987.

[24] L. B. Felsen and N. Marcuvitz, *Radiation and Scattering of Waves.* Englewood Cliffs, NJ: Prentice Hall, 1973.

[25] N. G. Alexopoulos, P. B. Katehi, and D. Rutledge, "Substrate optimization for integrated circuit applications," *IEEE Trans. Microwave Theory Tech.*, vol. MTT-31, pp. 550–557, July 1983.

[26] N. G. Alexopoulos and D. R. Jackson, "Fundamental superstrate (cover) effects on printed circuit antennas," *IEEE Trans. Antennas Propagat.*, vol. AP-32, pp. 807–814, Aug. 1984.

[27] P. B. Katehi and N. G. Alexopoulos, "Real axis integration of Sommerfeld integrals with applications to printed circuit antennas," *J. Math. Phys.*, vol. 24, no. 3, pp. 527–533, Mar. 1983.

[28] D. P. Kasilingam and D. B. Rutledge, "Surface-wave losses of coplanar waveguide transmission lines," *IEEE MTT-S. Int. Microwave Symp. Dig.*, 1993, pp. 113–115.

William P. Harokopus, Jr. (S'86–M'91) was born in Detroit, MI, on February 10, 1963. He received the B.S. (1985), M.S. (1986), and Ph.D. (1991) degrees in electrical engineering from the University of Michigan, Ann Arbor.

He is currently working in the Radiation Lab at the University of Michigan as a research engineer and is involved in the high-frequency modeling of monolithic millimeter-wave circuits and antennas.

Linda P. B. Katehi (S'81–M'84–SM'89) received the B.S.E.E. degree from the National Technical University of Athens, Greece, in 1977 and the M.S.E.E. and Ph.D. degrees from the University of California, Los Angeles, in 1981 and 1984 respectively.

In September 1984 she joined the faculty of the Electrical Engineering and Computer Science Department of the University of Michigan, Ann Arbor. Since then, she has been involved in the modeling and computer-aided design of millimeter-wave and near-millimeter-wave monolithic circuits and antennas.

In 1984 Dr. Katehi received the W. P. King Award and in 1985 the S. A. Schelkunoff Award from the Antennas and Propagation Society. In 1987 she received an NSF Presidential Young Investigator Award and an URSI Young Scientist Fellowship. She is a member of Sigma Xi.

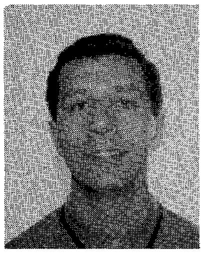

Walid Y. Ali-Ahmad (S'89) was born in Beirut, Lebanon, on November 29, 1966. He received the B.E. degree in electrical engineering (with distinction) from the American University of Beirut in 1988 and the M.S. degree in electrical engineering from the University of Michigan, Ann Arbor, in May 1990. He is currently a graduate student at the University of Michigan, Ann Arbor, working toward the Ph.D. in electrical engineering. He received the best paper award at the 1990 International Conference on Antennas, Nice, France. His research interests include millimeter-wave antennas and monolithic receivers.

Gabriel M. Rebeiz (S'86–M'88) was born in December 1964 in Beirut, Lebanon. He graduated in 1982 from the American University in Beirut with a B.E. (honors) in electrical engineering. In September 1982, he joined the California Institute of Technology, where he earned the Ph.D. degree in electrical engineering in June 1988.

He joined the faculty of the University of Michigan in September 1988 and is now an Assistant Professor there in the Electrical Engineering and Computer Science Department.

Dr. Rebeiz developed the integrated-horn antenna and was the recipient of a NASA Certificate of Recognition Award for his contribution to the millimeter-wave space program (March 1990). He also received the best paper award at the 1990 International Conference on Antennas, Nice, France. His research interests lie in planar millimeter-wave antennas and receivers and the fabrication of novel millimeter-wave transmission lines and devices.